Year-to-year variability in Hadley and Walker circulations from NCEP-NCAR reanalysis data

Shoshiro Minobe[1,2]

[1] Division of Earth and Planetary Sciences, Graduate School of Science, Hokkaido University, Sapporo, Japan.

[2] Frontier Research System for Global Change, Yokohama, Japan.

Submitted to the book entitled *"Hadley Circulation: Present, Past and Future"* (Eds R. S. Bradley and H. F. Dias), April 28, 2003, revised September 30, 2003.

Corresponding Author address:

Dr. Shoshiro Minobe
Division of Earth and Planetary Sciences,
Graduate School of Science,
Hokkaido University, Sapporo, 060-0810, Japan
e-mail: minobe@ep.sci.hokudai.ac.jp
Tel. +81-11-706-2644
Fax. +81-11-746-2715

Abstract

The year-to-year variability in the local Hadley and Walker circulations is studied by the EOF analysis of zonal and meridional divergent winds at 200 and 850 hPa of the NCEP/NCAR reanalysis data. The first mode of the EOF analysis since 1979 is closely related to El Nino/Southern Oscillation. The corresponding vertical velocity structure at the middle of the troposphere is characterized by the combination of a horseshoe in the western tropical Pacific and an oval in the central-eastern equatorial Pacific, consistent with satellite-derived precipitation correlations. A streamline analysis for horizontal divergent winds and vertical winds revealed that the dominant local Hadley and Walker circulation anomalies connect the oval and the horseshoe, while the other clusters of the local Hadley circulation anomalies rotating in opposing directions emanate from the Maritime Continent region.

The first EOF mode of the data from 1949 to 2002 is characterized by a trend-like increase from the 1960s to the 1980s consistent with the previous study by Goswami and Thomas (2000). This mode is accompanied by the increase of downward vertical wind anomalies over Sahel and over the central equatorial Pacific Ocean and by the increase of upward anomalies over the Maritime Continent and Amazon. Consistent precipitation decrease is observed over Sahel. Precipitation also decreased over the central Pacific, but the decrease region is located to the south of the center of the downward wind anomalies. Precipitation increases consistent with the local upward motions are not observed over the Maritime Continent or over the Amazon.

1. Introduction

The Hadley and Walker circulations are fundamental structures in the Earth's atmosphere, and hence their year-to-year variability is clearly of scientific value. The interannual changes of these circulation associated with El Niño/Southern Oscillation (ENSO) were intensively studied after pioneering works of Bjerkness (1966; 1969) by a number of papers (e.g.,; Arkin 1982; Webster et al. 1998; Philander 1990; Oort and Yienger, 1996; Wang, et al. 2000; Wang 2002ab). For understanding these circulation anomalies, schematic diagrams for the anomalous Walker circulation (e.g., McPhaden et al. 1998), and the combined Walker and local Hadley circulations (Wang 2002ab) were proposed. However, previous schematics may be insufficient to understand the three-dimensional nature of the anomalous Hadley and Walker circulations.

Recent advances in the atmosphere reanalysis data allow us to study more closely the Hadley and Walker circulations (e.g., Trenberth et al. 2000). Using NCEP/NCAR reanalysis data (Kalnay et al. 1996), Goswami and Thomas (2000) examined the three-dimensional decadal changes of Hadley and Walker circulations, and found that the most dominant changes are characterized by a trend from the 1960s to the 1980s. Focusing on El Niños on interannual timescale, Wang (2002a) proposed that anomalous local Hadley cells occur in the eastern and western Pacific rotating in opposing directions to each other, also using the NCEP/NCAR reanalysis data. Although these previous studies have provided useful information of interannual to interdecadal Hadley and Walker circulations, a number of questions should be still explored: Is the three-dimensional structure of Hadley and Walker circulation anomalies associated with ENSO well represented by the previous schematics? Is the trend robust regardless of analysis methods, and reasonably related to other field, i.e., precipitations? To address these questions, in the present paper, a combined EOF analysis of the 200- and 850-hPa divergent winds is performed.

The rest of the paper is organized as follows: in section 2, the data and methodology are described. The results of EOF analysis for the data for a period from 1979 to 2002, during which reanalysis data are more reliable than those in the earlier period, are explained in section 3. Using the whole record from 1949 to 2002, EOF analysis is repeated and its results are shown in section 4. In section 5, conclusions and discussion are presented.

2. Data and method

We mainly analyzed the NCEP/NCAR reanalysis data from January 1949 to April 2002 for divergent winds, upward velocities in pressure coordinates (minus ω), surface

temperatures, which are Sea-Surface Temperatures (SSTs) over the ocean and land surface temperatures otherwise (Kalnay et al.1996; Kistler et al., 2001). In order to obtain representative circulation changes related to the Hadley and Walker circulations, we calculate combined EOFs of four scalar variables (zonal and meridional divergent winds at 200 and 850 hPa) over the globe. This method would capture anomalies in *local* Hadley circulations and the Walker circulations. Structures of other fields, such as vertical wind speeds or surface temperatures, relating with the divergent wind EOFs are extracted by calculating correlation and regression coefficients of other fields onto the Principal Components (PCs) or the temporal coefficients of the EOFs.

The NCEP/NCAR reanalysis data are available from 1949, but the reliability of the earlier period of the record may be questionable due to smaller number of observations[1]. In particular, inclusion of satellite data since 1979 may substantially improve the reanalysis data. Thus, one of reasonable choices for the analysis period is from 1979 to the end of the record in 2002 as will be described in section 3. However, this choice can be too conservative so that we cannot obtain any information before 1979. Therefore, we will first examine EOF using the data after 1979 is examined in section 4.

In order to compare with the reanalysis vertical winds, we use a couple of precipitation datasets, since the reliability of the vertical velocities can be questionable (Kalnay et al. 1996; Newman et al. 2000). One dataset is Climate Prediction Center satellite/gauge Merged Analysis of Precipitation (referred to as CMAP data) (Xie and Arkin, 1997). The CMAP data used in the present study is a version in which the reanalysis precipitations were not incorporated. The other dataset is gridded land precipitations from gauge measurements (referred to as gauge data) (Dai et al., 1997). The period of the record are 1979–2002 for the CMAP data and 1850–1995 for the gauge data, respectively, though the gauge precipitation data are used for the overlapping period with the reanalysis data, i.e., from 1949 to 1995.

In addition to the above gridded data we use monthly El Niño SST indices, i.e., Niño 3, Niño 3.4, and Niño 4 indices since 1950. These Niño indices are obtained at the web-site of the Climate Prediction Center[2]. The Niño SST indices are area averaged SST anomalies from 1950 to 2002; The longitudinal ranges are 150°–90°W for Niño 3, 160°E–150°W for Niño 4, and 170°–120°W for Niño 3.4 index, with a common 5°S–5°N latitudinal range.

Anomalies of parameters are calculated as deviations of monthly climatologies, which are defined for the whole available records of respective data. The anomalies are averaged seasonally (sampling rate of three month) for smaller amount of computations for

---

[1] Number of sonde observations can be seen at

http://wesley.wwb.noaa.gov/cgi-bin/pdisp_m_obscnt.sh (Sept., 2003)

[2] http://www.cpc.ncep.noaa.gov/data/indices/

EOF analysis. Unless otherwise stated, raw seasonal anomalies are used.

3. EOF analysis since 1979

Figure 1ab shows the spatial patterns of the first EOF mode for the 200- and 850-hPa divergent zonal and meridional wind speeds. This mode explains 21% of the total variance of the divergent winds. The spatial structure is equivalent to the regression coefficients onto the PC-1. Also, accompanied regressions of vertical wind speeds at the middle of the troposphere are shown in Fig. 1c. Prominent divergences and convergences occur at the 200 hPa level over the tropical central-to-eastern Pacific and over the Maritime Continent, respectively. The divergence (convergence) in the upper troposphere is accompanied by convergence (divergence) in the lower troposphere, connected by the upward (downward) motions in the middle of the troposphere. The overall pattern of the vertical velocities can be viewed as a combination of a horseshoe pattern prevailing over the Maritime Continent and the subtropical western Pacific and an oval in the central-eastern tropical Pacific with opposing polarities.

Figure 1d shows correlation coefficients of surface temperatures onto the PC-1. The surface temperature chart is reminiscent of the typical SST anomaly pattern during the mature phase of ENSO (e.g., Rasmusson and Carpenter 1982). Consistently, the PC-1 captures the El Niño events in 1982/83, 1986/88, long-lasting El Niño in the early 1990s (Trenberth and Hoar 1996), and the latest event in 1997/98 (Fig. 2). The decorrelation time scale, which is given by the smallest lag with an auto-correlation smaller than e^{-1}, for the PC-1 is three seasons. Conservatively assuming that the data at one-year lag are independent, we find that an absolute correlation coefficient larger than 0.42 is significant at the 95% confidence limit. Correlation coefficients between the PC-1 and Niño SST indices are generally high, and the highest correlation (r=0.92) is found with the Niño 3.4 SST index followed by the second highest correlation (r=0.88) with the Niño 3 SST and by the correlation with the Niño 4 SST (r=0.82). This result indicates that dominant variability of the divergent winds, which are the most energetic in the tropics and hence represents the local Hadley and Walker circulations, is tightly related to the ENSO for the last two decades.

In order to obtain some idea for the reliability of the wind structures shown in Fig. 1, we compare the correlation coefficients of vertical winds onto the PC-1 and those of the CMAP-precipitations (Fig. 3). The combination of the horse-shoe and oval is commonly found in these correlation maps, but the extra-equatorial horse-shoe correlations in the Northern Hemisphere are weaker than those in the Southern Hemisphere. The correlation distribution for the precipitations is similar to the CMAP precipitation anomalies associated

with the Niño 3.4 SST variability shown by Wang et al. (2000). This is consistent with the close relation between the PC-1 and Niño 3.4 SST index.

Given the three-dimensional structure of horizontal divergent winds and vertical winds, it is not easy to understand these structures from Fig. 1 to the extent that we can confidently illustrate them by a schematic diagram. For a better understanding of those structures, we estimate streamlines according to the divergent winds and vertical winds. The streamline is defined as a curve for which the velocity field consisting of regressions of horizontal divergent and vertical winds onto the PC-1 is everywhere tangent. Streamlines can be illustrated in a three-dimensional plot as exemplified in Fig 4a, which shows streamlines starting from ±20°, 25° and 30° in latitude at the dateline and 500 hPa level for the EOF-1. These starting points correspond to the region of the large vertical velocities in the horseshoe pattern (Fig. 1). The streamlines connect the strong vertical wind regressions over the horseshoe pattern with the regressions with the opposing polarity over the equatorial oval pattern.

Although the three-dimensional view such as Fig. 4a is a powerful tool for exploring the shape of the streamlines in detail, it is not possible to draw a large number of streamlines (i.e., more than 10) in a panel. Thus, to display an overall pattern of the streamlines, we employ a plain view like Fig. 4b, but with a much larger number of streamlines.

Figure 5 shows the plain view of streamlines associated with the EOF-1 starting at every 10° in longitude and 5° in latitude between 40°S and 40° N and at 500 hPa. To avoid making the figure panel too busy and to focus on important streamlines, we plot only streamlines that are accompanied by absolute values of vertical velocities larger than 0.002 Pa s^{-1} at the starting points, and reach 300 or 700 hPa level. The streamlines that meet these conditions are mostly limited to the Indian Ocean and the Pacific Ocean, and exhibit a well organized, meridionally symmetric pattern. In the Pacific Ocean, the streamlines run over the tropical North (South) Pacific in northwest-southeast (northeast-southwest) direction, and these streamlines connect the region of active vertical motions in the central Pacific Ocean and those in the subtropical western North and South Pacific. From another equatorial divergent center located over the Maritime Continent, streamlines emanate to the westward, northwestward, southwestward and eastward. The eastward branch of streamlines from the Maritime Continent towards the dateline represents the Walker circulation anomalies. Also, the Walker circulation anomalies are expressed by the bending of streamlines in the central Pacific; In this region, strong zonal wind anomalies trapped near the equator bend streamlines, which extend from off-equator toward the equator according to the local Hadley circulation, in the zonal direction near the equator. Thus, the equatorial bending indicates that substantial Walker and local Hadley circulation anomalies coexist over the central equatorial Pacific. The other divergence center over the eastern Amazon and western equatorial Atlantic is connected to the eastern Pacific by streamlines directly. That is, in this region Walker circulation anomalies are much more pronounced than local Hadley circulation anomalies around the

equator, consistent with Wang (2002b; 2003). These features are summarized in the schematic diagram in Fig. 6.

The present diagram in Fig. 6 is similar to the diagram of Wang (2002a) with respect to the fact that the two anomalous local Haley circulations occur in the central-eastern Pacific and in the Maritime Continent with opposing polarity. However, the present diagram emphasizes the meridionally slanted nature of the divergent winds, and dominance of the local Hadley circulations over the central-eastern Pacific Ocean. The overwhelming local Hadley circulations over the central-eastern Pacific Ocean compared to the opposing local Hadley circulations over the Maritime Continent results in the symmetric structures of the global Hadley circulation anomalies associated with ENSO reported by previous studies (Oort and Yienger 1996; Goswami and Thomas 2000).

In order to know whether the streamlines (Fig. 5), which are the basis of the schematic diagram of Fig. 6, are robust with respect to the details of the analysis method, we calculated streamlines based on regression coefficients with Niño 3.4 index using the data since 1979 (not shown) and using the data since 1950 (Fig. 7a). As expected from the high correlation between the PC-1 and Niño 3.4, the streamlines based on regression coefficients with Niño 3.4 index are quite similar to those with the PC-1 (No essential difference was found according to the different periods of regression calculations.). Furthermore, streamlines are calculated based on a composite of ENSO-mature phase (Fig. 7b). The composite is calculated from November to the next January for seven significant El Niño events (1957/58, 1965/66, 1972/73, 1982/83, 1986/87, 1991/92 and 1997/98) according to Wang et al. (2002a). The streamlines for the ENSO mature phase are less symmetric about the equator than those for the EOF-1, with more (less) prominent zonal streamlines in the Northern (Southern) Hemisphere. Except for this difference, the overall structure is common between the streamlines for the ENSO composite and those for the EOF-1. Therefore, it can be concluded that the schematic diagram shown in Fig. 6 is not substantially dependent on the details of the analysis methods, and captures the dominant structures of the Haley and Walker circulation anomalies associated with ENSOs.

4. EOF analysis since 1949

When we calculate the EOFs using divergent winds since 1949 instead of 1979 in the previous section, we found that the PC-1 since 1949 is entirely different from the aforementioned PC-1 since 1979 with a correlation coefficient as low as 0.05 for the overlapping period from 1979 to 2002. The PC-1 since 1949 is characterized by a long-term increase from the 1960s to the 1980s (Fig. 8). The EOF-1 explains 24% of the total variance of the 200- and 850-hPa divergent winds.

Figure 9a–c shows that the spatial pattern of the divergent winds for the EOF-1 is characterized by the lower-level divergence (upper-level convergence) over the tropical Pacific, the Amazon, central Africa, and the Maritime Continent, with alternating polarities. Again, the lower level divergence (convergence) is accompanied by the upper level convergence (divergence) and downward (upward) vertical winds in the middle of the troposphere. The strong correlations of surface temperatures are found over the tropical Indian Ocean-Maritime Continent with smaller correlations over Africa and the tropical South Atlantic (Fig. 9d).

Figure 10a shows a time series comparison between the PC-1 and the tropical Indian Ocean-Maritime Continent SST. The Indian Ocean-Maritime Continent SST appears as an abrupt warming in the 1970s rather than a continuous increase as in the PC-1. The abrupt warming is known as a part of the 1970s climatic regime shift (Nitta and Yamada 1989; Trenberth 1990). Minobe (1997) reported that the occurrences of other two climatic regime shifts in the 1920s and 1940s, and that these two regime shifts are also accompanied by consistent SST changes over the tropical Indian Ocean-Maritime Continent.

The present result is consistent with the analysis of Goswami and Thomas (2000), who examined EOFs of total wind fields (not divergent winds) combined with other fields. Their temporal coefficient also exhibited prominent increase from the 1960s to the 1980s, and spatial structure of the total wind anomalies is similar to those of the present study (not shown). It is noteworthy, however, the PC-1 of Goswami and Thomas (2000) returned to around zero at the end of their record (1996) from the maximum in the late 1980s, but the PC-1 in the present study stays high from the 1980s to the end of the record (2002). This discrepancy may arise from an end effect of the low-pass filtering employed by Goswami and Thomas (2000), or partly from the longer record used in the present study than that used in their study.

Figure 11 shows the correlations of vertical winds with the PC-1 and those of the gauge precipitations. As described in section 2, the reliability of the earlier record of the NCEP/NCAR reanalysis data can be questionable, and hence we need to be careful about the trend found in the PC-1 by the EOF analysis from 1949. The increasing downward wind anomalies expressed by negative correlations around Sahel are consistent with the negative correlations of precipitations, which are related to previously reported decreasing Sahel rainfalls (e.g., Zheng et al. 1999). Figure 10b shows that the Sahel rainfall decrease mainly occurred from the 1970s to the 1980s, roughly the same period of the prominent change of the PC-1. The increasing downward anomalies over the equatorial central Pacific might be related to the negative correlations in the precipitations over the tropical South Pacific, though the location of the latter is shifted to the south of the former (Fig. 11). Very recently, examining the observed data in Comprehensive Ocean-Atmosphere Data Set (COADS), Evans and Kaplan (2003) showed that quantitatively similar trends are observed both in the NCEP-NCAR reanalysis data and COADS data over the Pacific Ocean. In contrast to some

supports from the precipitations for those downward wind anomalies of the trend, the upward anomalies over the Amazon and over the Maritime Continent are not accompanied by the increases of rainfalls. Consequently, some trends in Hadley and Walker circulations may have occurred in the late 20th century associated with the precipitation trends over Africa and over the tropical Pacific Ocean, but the detail of the structure of the circulation anomalies may be different from that shown in Fig. 10.

It is noteworthy that the EOF-2 since 1949 is virtually identical to the EOF-1 of the analysis since 1979 with a remarkably high correlation between the PC-2 since 1949 and PC-1 since 1979 (r=0.98). Also, the correlation between the Niño 3.4 SST and the PC-2 since 1949 is as high as 0.89. This indicates that the ENSOs influence the NCEP-NCAR reanalysis data in a similar manner throughout the record.

5. Conclusions and discussion

The year-to-year variability of local Hadley and Walker circulations are studied. A combined EOF analysis of 200- and 850-hPa zonal and meridional divergent winds of the NCEP/NCAR reanalysis data has shown a close relation between the ENSOs and local Hadley and Walker circulation anomalies, depicted as the first mode by the EOF analysis since 1979 and as the virtually identical second mode by the analysis since 1949. The vertical wind anomalies in the middle of the troposphere are characterized by the oval pattern in the central-eastern equatorial Pacific and the horseshoe pattern with a opposing polarity over the tropical western Pacific. The regression fields of the vertical winds and horizontal divergent winds are analyzed with streamlines of these wind fields; it turned out that the streamlines connect the oval and horseshoe patterns. The major features of the streamlines are summarized in a schematic diagram (Fig. 6). The robustness of the streamline analysis is confirmed by a regression analysis with the Niño 3.4 index and by a composite analysis for ENSO events. The present schematic is consistent with Wang's (2002a) schematic for the ENSO mature phase with respect to the two anomalous local Haley circulations occurring in the central-eastern Pacific and in the western Pacific with opposing polarity, but the present diagram emphasizes the meridionally slanted nature of the divergent winds, and dominance of the local Hadley circulations over the central-eastern Pacific Ocean.

The first mode of the EOF analysis since 1949 exhibits a strong trend from the 1960s to the 1980s, consistent with Goswami and Thomas (2000). The upward wind anomalies over Sahel of the trend are consistent with the Sahel rainfall decrease, and upward anomalies over the central equatorial Pacific can be related to the precipitation decrease over the tropical South Pacific. However, precipitation anomalies consistent with the upward anomalies are observed neither over the Amazon nor over the Maritime Continent.

The local Hadley and Walker circulation anomalies are essential for socio-economic impacts especially via precipitation anomalies (e.g., Webster et al. 1998; Wang et al. 2000),

but the global Hadley circulation may be useful for basic understanding of the physical mechanism. For example, Seager et al. (2003) recently proposed that the ENSO events cause global Hadley circulation anomalies symmetric to the equator due to tropical heating and mid-latitude wave mean-flow interactions, based on a zonally averaged momentum flux analysis. The present result indicates the dominance of the local Hadley circulation anomalies over the central-to-eastern tropical Pacific, which is related to the global Hadley circulation anomalies studied by Oort and Yienger (1996).

The Hadley circulations are important to connect the equator and mid-latitudes. The present paper has focused on the ENSO and the trend, but the influences of the equatorial variability on the mid-latitudes were also proposed for decadal variability over the Pacific Ocean (e.g., Graham 1994; Gu and Philander 1997; Mantua et al. 1997; Luo and Yamagata 2001; Bratcher and Giese 2002; Newman et al. 2003). The one of the most interesting decadal variability in the Pacific Ocean may be the Pacific (inter-)Decadal Oscillation (PDO) (Mantua et al. 1997; Mantua and Hare 2002). Zhang et al. (1997) suggested that the ENSO-like decadal mode, which is closely related to the PDO, is accompanied by less pronounced Hadley circulation anomalies than the ENSO mode. Furthermore, for the PDO, two dominant timescales were proposed; one is 50–70-yr oscillation (Minobe 1997) and the other is about 20-yr oscillation (Mann and Park 1996; Minobe 1999, 2000; Minobe et al. 2002). Recently, Minobe and Nakanowatari (2002) showed that the 20-yr variability exerts substantial influence on precipitations over the Pacific Ocean, and suggested that the Hawaii winter droughts are strongly related to the 20-yr oscillation. Further studies in future are necessary to understand the roles of the Hadley and Walker circulations in the climate system on various timescales.

Acknowledgements

The author thanks H. Diaz and R. Bradley for inviting me to participant to this book and to the closely relating workshop, C. Wang, M. Evans and I. Dima for invaluable discussion, N. Harnik for a preprint. This study is supported by grants from the Japanese Ministry of Education, Culture, Sports, Science and Technology.

References

Arkin A. 1982: The relationship between interannual variability in the 200mb tropical wind field and the Southern Oscillation. *Mon. Wea. Rev.*, **110**, 1393-1404.

Bjerkness, J. 1966: A possible response of the atmospheric Hadley circulation to equatorial anomalies of ocean temperature. *Tellus*, **18**, 820–829.

Bjerkness, J. 1969: Atmospheric teleconnections from the equatorial Pacific. *Mon. Wea. Rev.*, **97**, 164–172.

Bratcher A. J. and B. S. Giese, 2002: *Geophys. Res. Lett.*, **29**, 1918, doi: 10.1029/2002GL015191.

Dai, A., I. Y. Fung, and A. D. D. Genio, 1997: Surface observed global land precipitation variations during 1900–1988. *J. Climate*, **10**, 2943–2962.

Deser, C. and M. L. Blackmon, 1995: On the relationship between tropical and North Pacific sea surface temperature variations. *J. Climate*, **8**, 1677-1680.

Evans, M. N., and A. Kaplan, 2003: Hadley and Walker circulation variability in historical marine wind analyses: Potential for paleo-reconstructions from proxy data. *Hadley Circulation: Present, Past and Future*, Eds R. S. Bradley and H. F. Dias, (this volume).

Goswami, B. N. and M. A. Thomas, 2000: Coupled ocean-atmosphere inter-decadal modes in the tropics. *J. Meteorol. Soc. Jpn.*, **78**, 765–775.

Graham, N.E. 1994: Decadal scale variability in the 1970's and 1980's: Observations and model results. *Clim. Dy.* **10**, 135-162.

Gu, D. F., and S. G. H. Philander, 1997: Interdecadal climate fluctuations that depend on exchanges between the tropics and extratropics. *Science*, **275**, 805-807.

Kalnay, E., M. Kanamitsu, R. Kistler, W. Collins, D. Deaven, L. Gandin, M. Iredell, S. Saha, G. White, J. Woollen, Y. Zhu, A. Leetmaa, B. Reynolds, M. Chelliah, W. Ebisuzaki, W. Higgins, J. Janowiak, K.C. Mo, C. Ropelewski, J. Wang, R. Jenne and D. Joseph, 1996: The NCEP/NCAR 40-Year Reanalysis Project. *Bull. Amer. Meteor. Soc.*, **77**, 437-472.

Kistler, R., E. Kalnay, W. Collins, S. Saha, G. White, J. Woollen, M. Chelliah, W. Ebisuzaki, M. Kanamitsu, V. Kousky, H. van den Dool, R. Jenne, and M. Fiorino, 2001: The NCEP-NCAR 50-year reanalysis: Monthly means CD-ROM and Documentation, Bull. Am. Met. Soc., 82, 247-268.

Luo J. J., Yamagata T, 2001: Long-term El Nino-Southern Oscillation (ENSO)-like variation with special emphasis on the South Pacific. J. Geophys. Res., 106 (C10), 22211-22227.

Mann, M. E., and J. Park, 1996: Joint spatiotemporal modes of surface temperature and sea level pressure variability in the Northern Hemisphere during the last century. *J. Climate,* **9**, 2137-2162.

Mantua, N. J., S. R. Hare, Y. Zhang, J. M. Wallace, and R. C. Francis, A Pacific interdecadal climate oscillation with impacts on salmon production. *Bull. Am. Met. Soc.*, **76**, 1069–1079, 1997.

McPhaden M. J., A. J. Busalacchi, R. Cheney, J.-R. Donguy, K. S. Gage, D. Halpern, M. Ji, P. Julian, G. Meyers, G. T. Mitchum, P. P. Niiler, J. Picaut, R. W. Reynolds, N. Smith, and K. Takeuchi, 1998: The tropical ocean-global atmosphere observing system: A decade of progress. *J. Geophys. Res.*, **103 (C7)**, 14,169–14,240.

Minobe, S., 1997: A 50–70 year climatic oscillation over the North Pacific and North America. *Geophs. Res. Lett.*, **24**, 683–686.

Minobe, S., 1999: Resonance in bidecadal and pentadecadal climate oscillations over the North Pacific: Role in climatic regime shifts. *Geophys. Res. Lett.*, **26**, 855–858.

Minobe, S., 2000: Spatio-temporal structure of the pentadecadal variability over the North Pacific. *Progr. Oceanogr.*, **47**, 99–102.

Minobe, S., T. Manabe, and A. Shouji, 2002: Maximal wavelet filter and its application to bidecadal oscillation over the Northern Hemisphere through the 20th century. *J. Climate*, **15**, 1064–1075.

Minobe, S. and T. Nakanowatari, 2002: Global structure of bidecadal precipitation variability in boreal winter, *Geophys. Res. Lett.* **29 (10),** 10.1029/2001GL014447.

Newman M., P. D. Sardeshmukh, and J. W. Bergman, 2000: An assessment of the NCEP, NASA and ECMWF reanalyses over the Tropical West Pacific warm pool. Bull. Amer. Meteor. Soc., 81, 41-48.

Newman, M., G. P. Compo, M. A. Alexander, 2003: ENSO-forced variability of the Pacific Decadal Oscillation. J. Climate, in press.

Nitta, T., and S. Yamada, 1989: Recent warming of tropical sea surface temperature and its relationship to the Northern Hemisphere circulation. *J. Meteor. Soc. Japan*, **67**, 375-383.

Oort A. H., and J. J. Yienger, 1996: Observed interannual variability in the Hadley circulation and its connection to ENSO. *J. Climate*, **9**, 2751–2767.

Philander S. G., 1990: *El Niño and La Niña and the Southern Oscillation.* Academic Press, 289 pp.

Rasmusson, E. M., and T. H. Carpenter, 1982: Variations in tropical sea surface temperature and surface wind fields associated with the Southern Oscillation-El Nino. *Mon. Wea. Rev.*, **110**, 354–384.

Seager, R., N. Harnik, Y. Kushnir, W. Robinson, and J. Miller, 2003: Mechanisms of hemispherically symmetric climate variability. *J. Climate*, submitted.

Trenberth, K. E., 1990: Recent observed interdecadal climate changes in the Northern Hemisphere. *Bull. Am. Met. Soc.*, **71**, 988-993.

Trenberth, K. E., and T. J. Hoar, 1996: The 1990-1995 El Nino-Southern Oscillation event: Longest on record. *Geophys. Res. Lett.*, **23**, 57-60.

Trenberth, K. E., D. P. Stepaniak, and J. M. Caron, 2000: The global monsoon as seen through the divergent atmospheric circulation. *J. Climate*, **13**, 3969–3993.

Wang B., R. Wu, and X. Fu, 2000: Pacific-East Asian teleconnection: How does ENSO affect East Asian climate*? J. Climate*, **13**, 1517–1536.

Wang C., 2002a: Atmospheric circulation cells associated with the El Nino-Southern Oscillation. *J. Climate*, **15**, 399–419.

Wang C., 2002b: Atlantic climate variability and its associated atmospheric circulation cells. *J. Climate*, **15**, 1516–1536.

Wang C., 2003: ENSO, Atlantic climate variability, and the Walker and Hadley Circulations. *Hadley Circulation: Present, Past and Future*, Eds R. S. Bradley and H. F. Dias, (this volume)

Webster, P. J., V. O. Magaña, T. N. Palmer, J. Shukla, R. A. Tomas, M. Yanai, and T. Yasunari,

1998: Monsoons: Processes, predictability, and the prospects for prediction. *J. Geophys. Res.*, **103 (C7)**, 14,451–14,510.

Zeng, N., J. D. Neelin, K.-M. Lau, and C. J. Tucker, 1999: Enhancement of interdecadal climate variability in the Sahel by vegetation interaction. *Science*, **286**, 1537–1540.

Zhang, Y., J. M. Wallace, and D. S. Battisti, 1997: ENSO-like interdecadal variability: 1900-93. *J. Climate*, **10**, 1004-1020.

Figure Captions

Figure 1. Spatial structures of the 1st combined EOF mode of 200- and 850-hPa divergent winds from 1979 to 2002. Panel (a) and (b) show the EOF1, which is equivalent to regressions onto the PC-1, of the 200 hPa (a) and 850 hPa (b) divergent winds, respectively. Panel (c) shows the regression coefficients of upward vertical velocity in the pressure coordinate at 500 hPa onto the PC-1 in units of 1×10^{-3} Pa s^{-1}, and panel (d) shows correlation coefficients of SSTs onto the PC-1 in tens. For panel (c), contour interval is 2×10^{-3} Pa s^{-1} without zero contours and shading indicates the regions where the absolute values are larger than 4×10^{-3} Pa s^{-1}. For panel (d), contour interval is 1 in tens (0.1 for correlations) for absolute correlations larger than 0.3, and shading indicates the regions where the absolute values of correlations are larger than 0.4.

Figure 2. First Principal Component (PC-1) or the time coefficient of the EOF-1 shown in Fig. 1 (black line) and Niño 3.4 SST index in arbitrary units (gray line).

Figure. 3. (a) Correlations of the upward vertical velocity in the pressure coordinate at 500 hPa onto the PC-1, which is shown in Fig. 2, and (b) correlations of the CMAP precipitations onto the PC-1. Units are tens, and contour interval is 0.1 for absolute correlations larger than 0.3.

Figure. 4. Bird's-eye view (a) and plain view(b) of streamlines according to the regression coefficients of the divergent horizontal winds and vertical winds (see text), starting from ±20°, 25°, and 30° in latitude at the dateline and at 500 hPa level. Black and gray curves indicate streamlines located above and below 500 hPa height, respectively.

Figure 5. Streamlines corresponding to the horizontal divergent winds and vertical winds shown in Figs. 1. The streamlines start at 500 hPa level at every 10° in longitudes and 5° in latitudes, traced until the stream line again crosses 500 hPa. Streamlines are not shown, if the streamline that are accompanied by the absolute vertical wind regression at the starting point smaller than 0.002 Pa s^{-1} or the streamline does not reach 300 or 700 hPa level. Black and gray curves indicate streamlines located above and below 500 hPa height, respectively.

Figure 6. Schematics for structures of horizontal divergent and vertical wind speeds for the EOF-1 from 1979 to 2002 drawn based on Figs. 1, 4 and 5.

Figure. 7. Same as Fig. 5, but for streamlines (a) based on regression coefficients of divergent winds and vertical winds with the Niño 3.4 SST index, and (b) based on the ENSO

mature-phase composite (see text).

Figure 8. PC-1 of the EOF analysis of divergent winds from 1949 to 2002.

Figure 9. Same as Fig. 1, but for the EOF analysis using the data from 1949 to 2002.

Figure 10. Time series comparison of tropical Indian Ocean-Maritime Continent SST anomalies (60°–150°E, 10°S–10°N) (gray line, top panel), Sahel precipitation anomalies (20°W–30°E 5°–20°N) (gray line, bottom panel) and the PC-1 since 1949, which was also shown in Fig. 8 (black line, both panels). The Sahel precipitation time series is smoothed by three-point running mean and the other time series are unfiltered (raw seasonally sampled anomalies). The axis of the precipitation is reversed for an easier comparison.

Figure. 11. (a) Correlations of the upward vertical velocity in the pressure coordinate at 500 hPa onto the PC-1 since 1949, which is shown in Fig. 8, and (b) correlations of the gauge precipitations onto the PC-1.

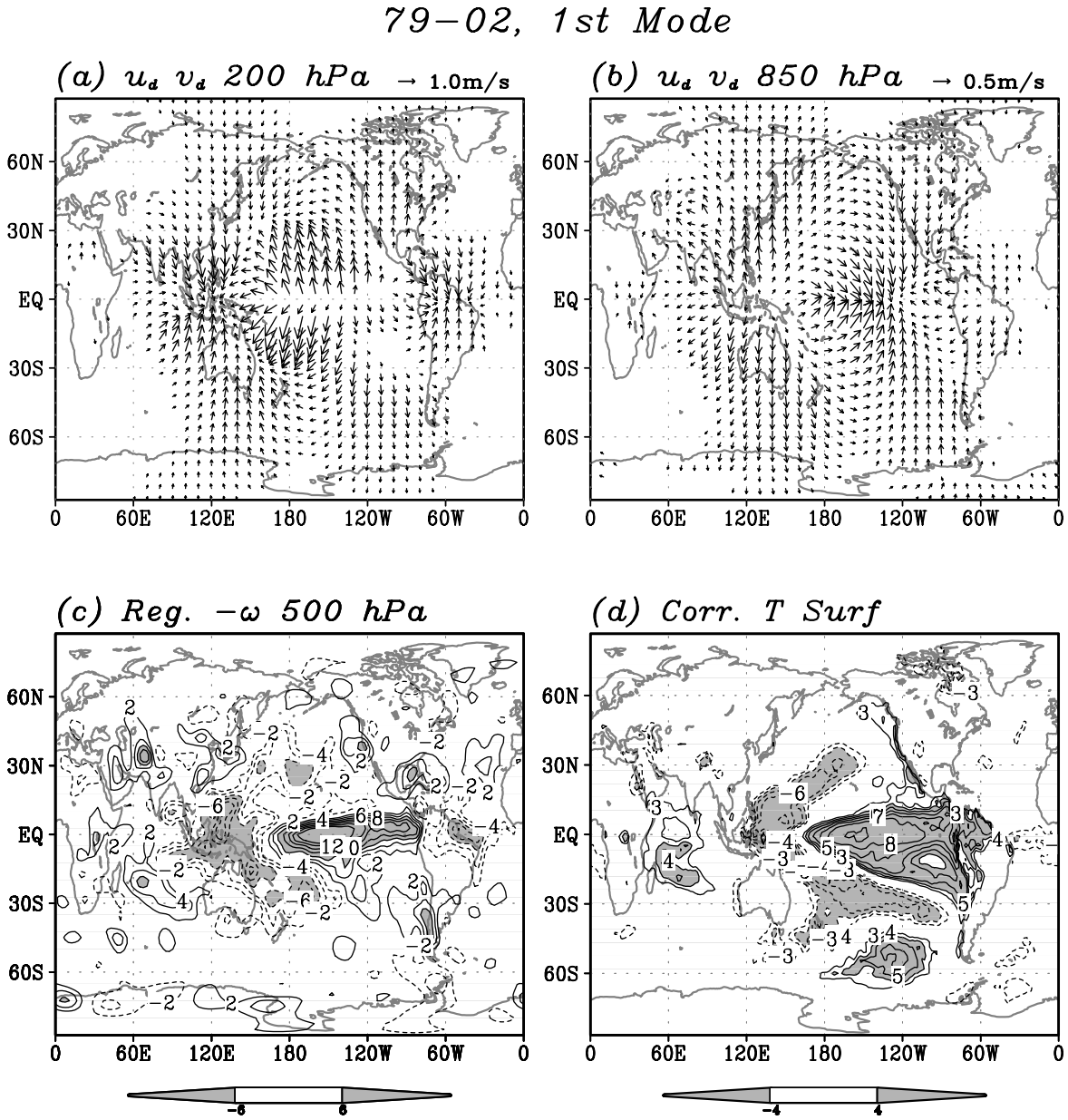

Figure 1. Spatial structures of the 1st combined EOF mode of 200- and 850-hPa divergent winds from 1979 to 2002. Panel (a) and (b) show the EOF1, which is equivalent to regressions onto the PC-1, of the 200 hPa (a) and 850 hPa (b) divergent winds, respectively. Panel (c) shows the regression coefficients of upward vertical velocity in the pressure coordinate at 500 hPa onto the PC-1 in units of 1×10^{-3} Pa s^{-1}, and panel (d) shows correlation coefficients of SSTs onto the PC-1 in tens. For panel (c), contour interval is 2×10^{-3} Pa s^{-1} without zero contours and shading indicates the regions where the absolute values are larger than 4×10^{-3} Pa s^{-1}. For panel (d), contour interval is 1 in tens (0.1 for correlations) for absolute correlations larger than 0.3, and shading indicates the regions where the absolute values of correlations are larger than 0.4.

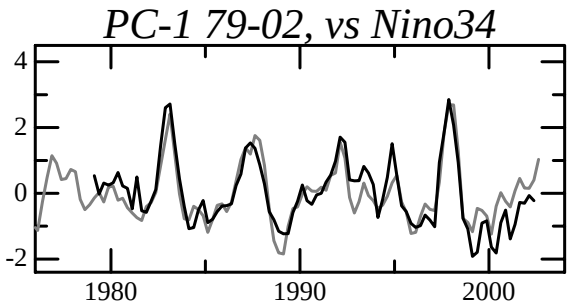

Figure 2. First Principal Component (PC-1) or the time coefficient of the EOF-1 shown in Fig. 1 (black line) and Niño 3.4 SST index in arbitrary units (gray line).

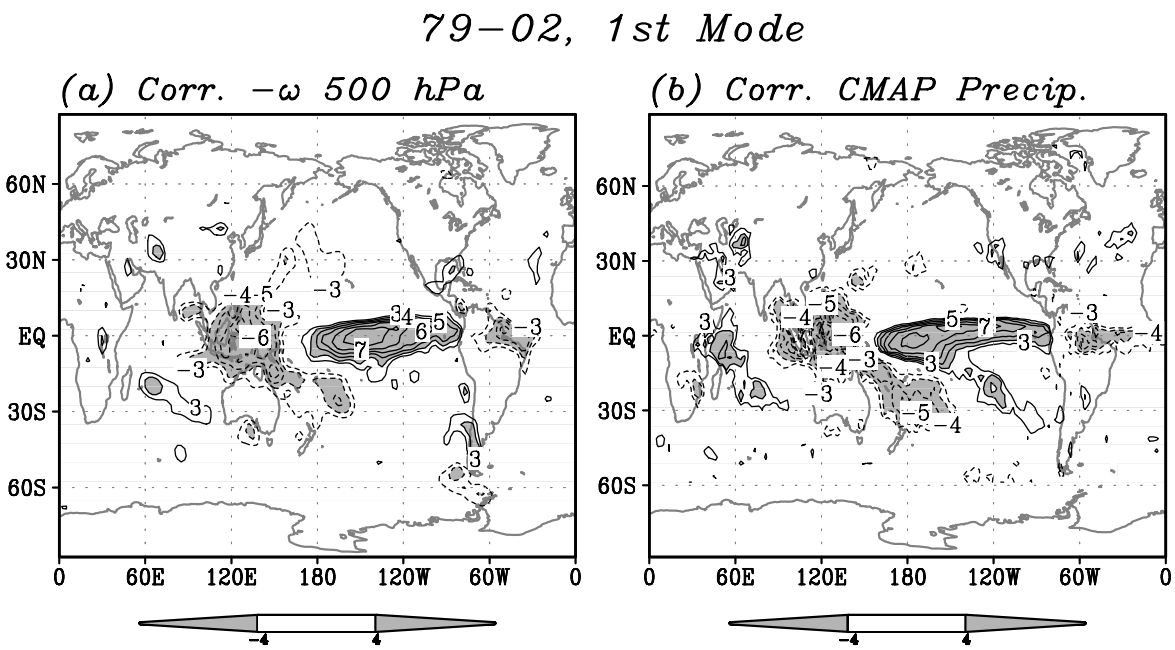

Figure. 3. (a) Correlations of the upward vertical velocity in the pressure coordinate at 500 hPa onto the PC-1, which is shown in Fig. 2, and (b) correlations of the CMAP precipitations onto the PC-1. Units are tens, and contour interval is 0.1 for absolute correlations larger than 0.3.

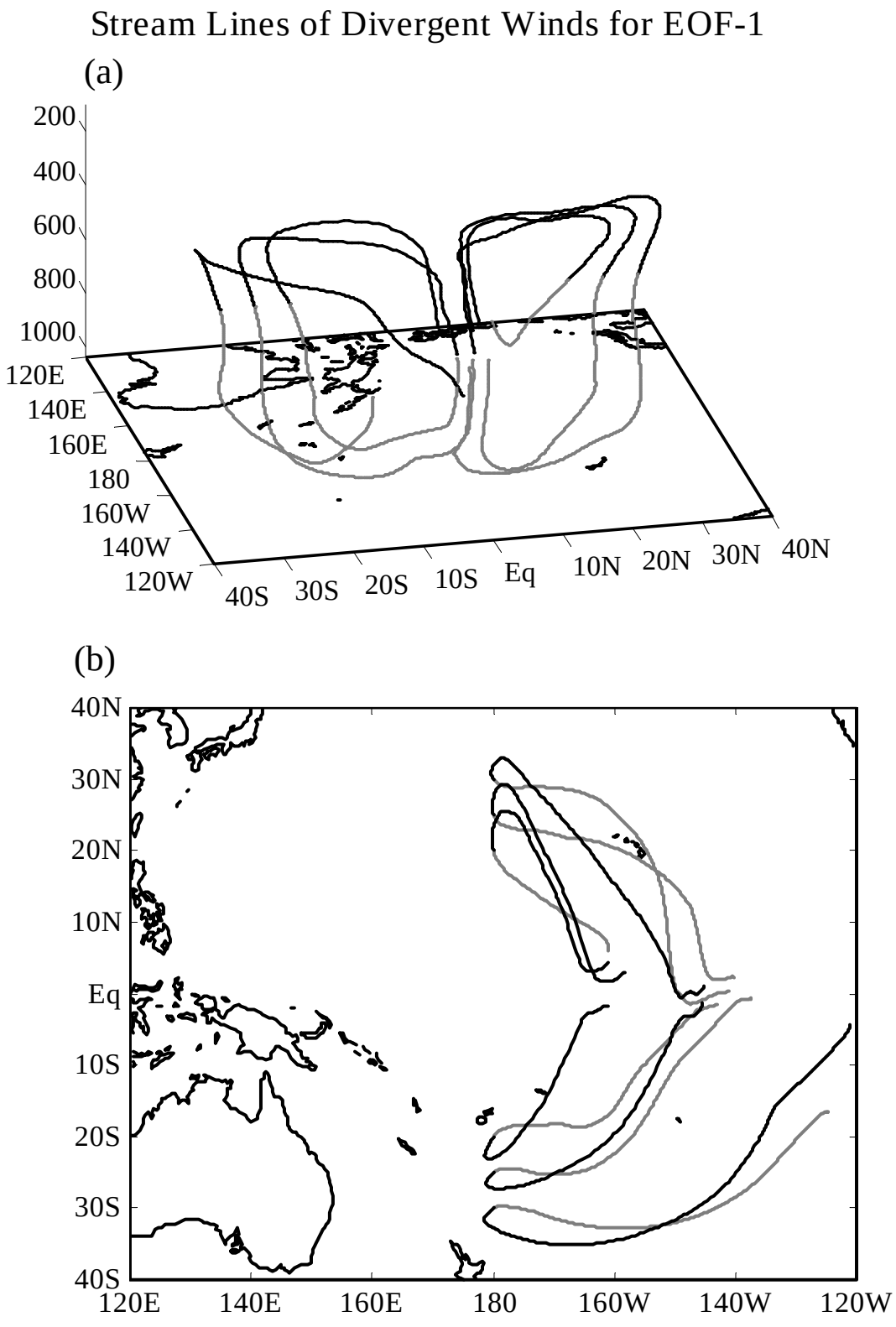

Figure. 4. Bird's-eye view (a) and plain view(b) of streamlines according to the regression coefficients of the divergent horizontal winds and vertical winds (see text), starting from ±20°, 25°, and 30° in latitude at the dateline and at 500 hPa level. Black and gray curves indicate streamlines located above and below 500 hPa height, respectively.

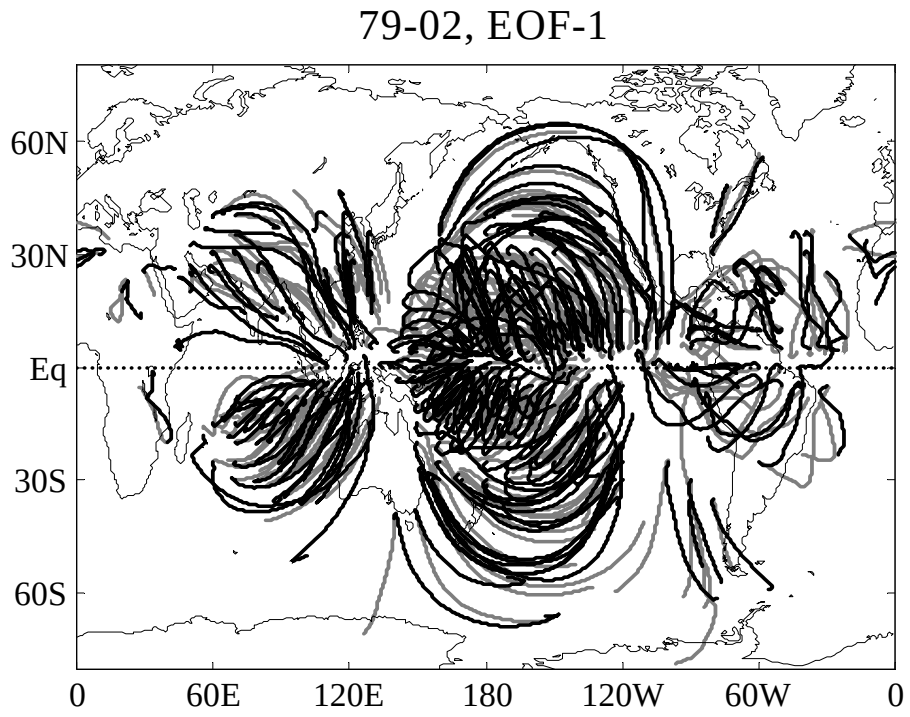

Figure 5. Streamlines corresponding to the horizontal divergent winds and vertical winds shown in Figs. 1. The streamlines start at 500 hPa level at every 10° in longitudes and 5° in latitudes, traced until the stream line again crosses 500 hPa. Streamlines are not shown, if the streamline that are accompanied by the absolute vertical wind regression at the starting point smaller than 0.002 Pa s^{-1} or the streamline does not reach 300 or 700 hPa level. Black and gray curves indicate streamlines located above and below 500 hPa height, respectively.

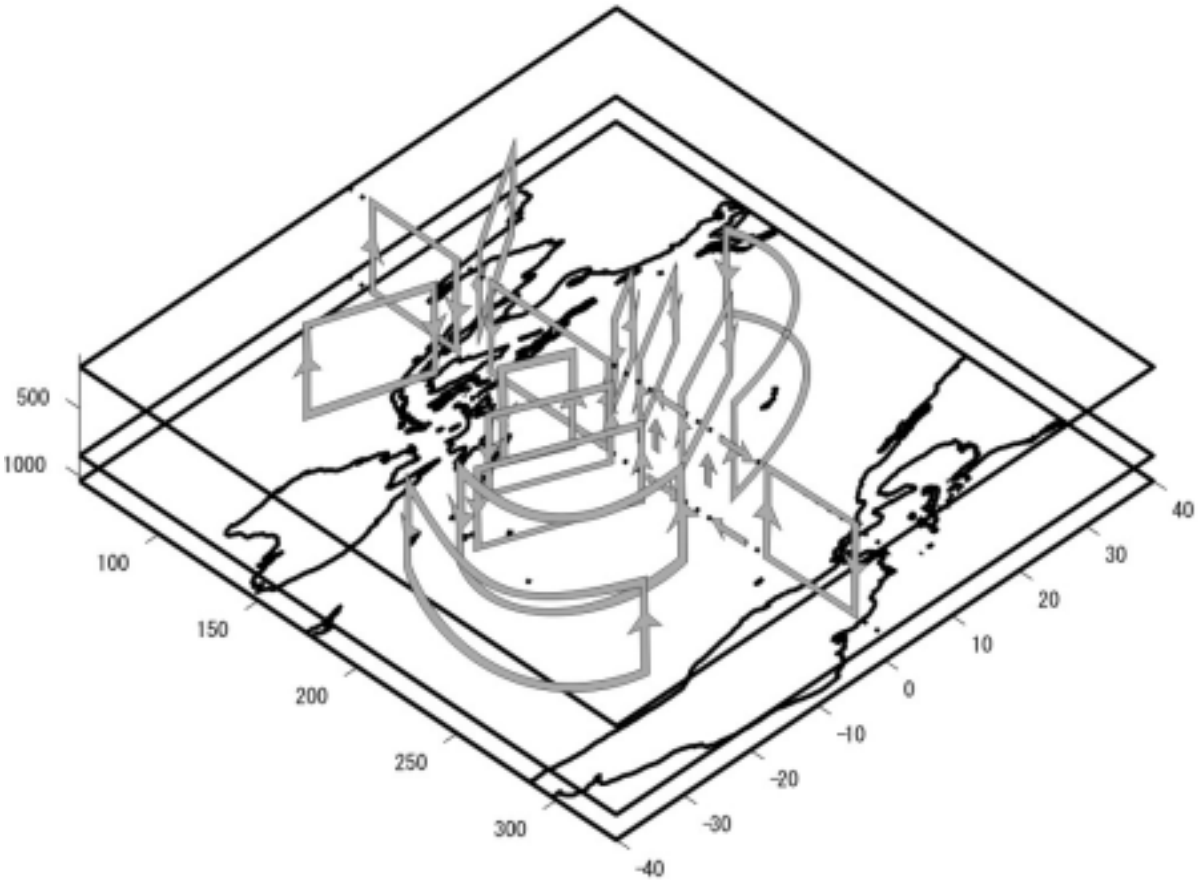

Figure 6. Schematics for structures of horizontal divergent and vertical wind speeds for the EOF-1 from 1979 to 2002 drawn based on Figs. 1, 4 and 5.

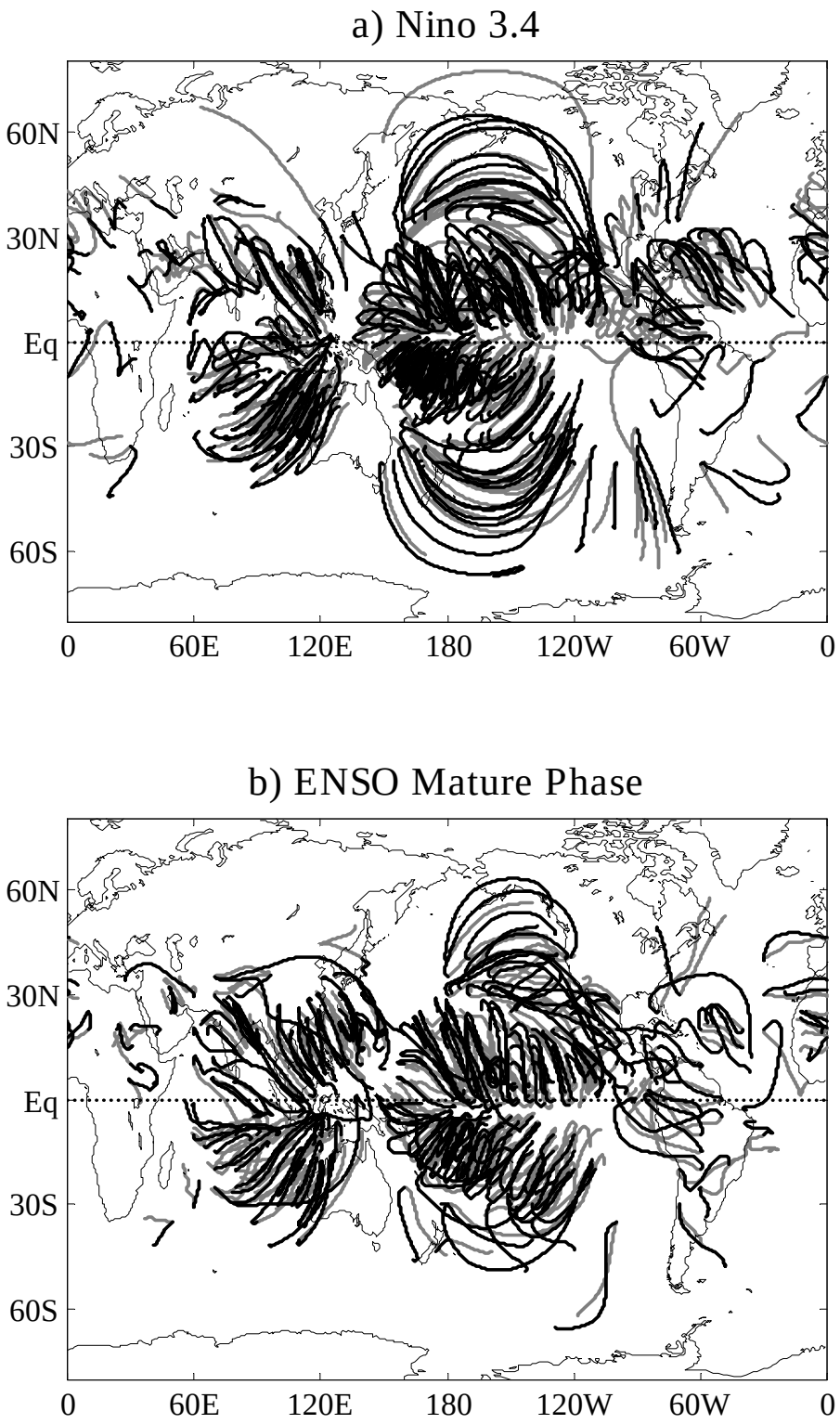

Figure. 7. Same as Fig. 5, but for streamlines (a) based on regression coefficients of divergent winds and vertical winds with the Niño 3.4 SST index, and (b) based on the ENSO mature-phase composite (see text).

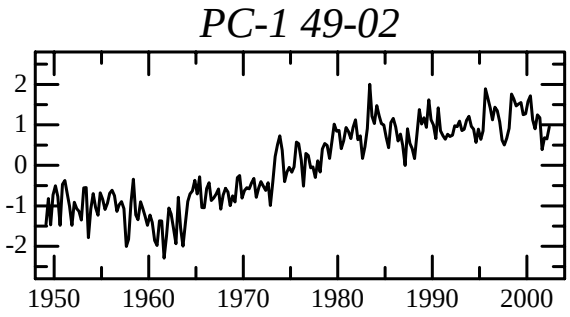

Figure 8. PC-1 of the EOF analysis of divergent winds from 1949 to 2002.

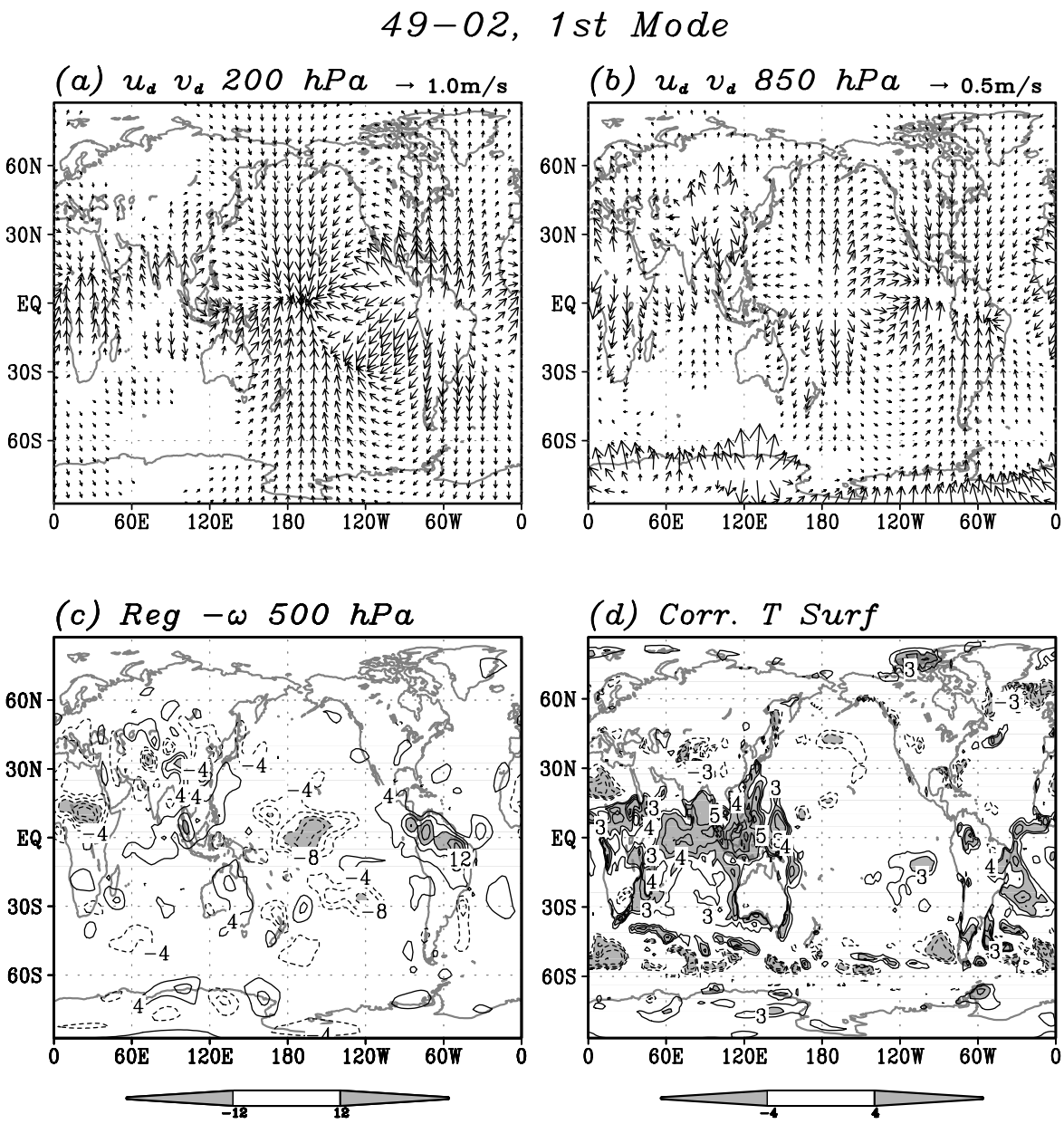

Figure 9. Same as Fig. 1, but for the EOF analysis using the data from 1949 to 2002.

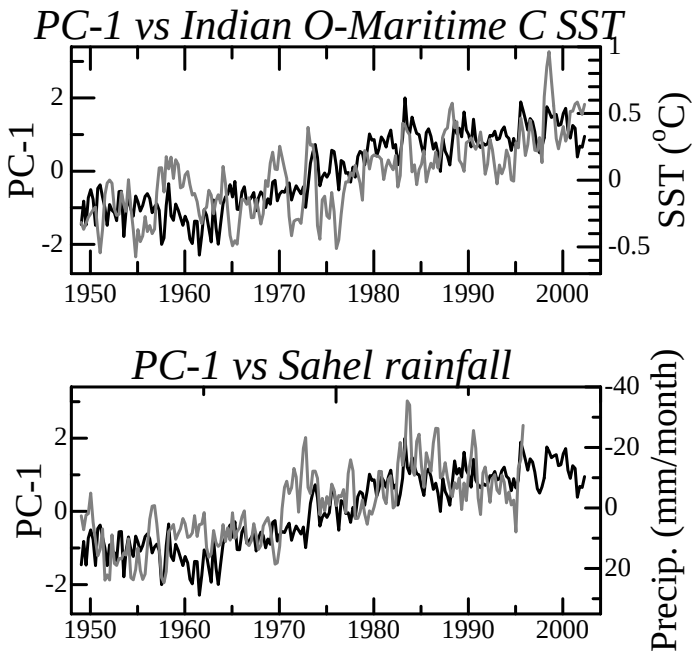

Figure 10. Time series comparison of tropical Indian Ocean-Maritime Continent SST anomalies (60°–150°E, 10°S–10°N) (gray line, top panel), Sahel precipitation anomalies (20°W–30°E 5°–20°N) (gray line, bottom panel) and the PC-1 since 1949, which was also shown in Fig. 8 (black line, both panels). The Sahel precipitation time series is smoothed by three-point running mean and the other time series are unfiltered (raw seasonally sampled anomalies). The axis of the precipitation is reversed for an easier comparison.

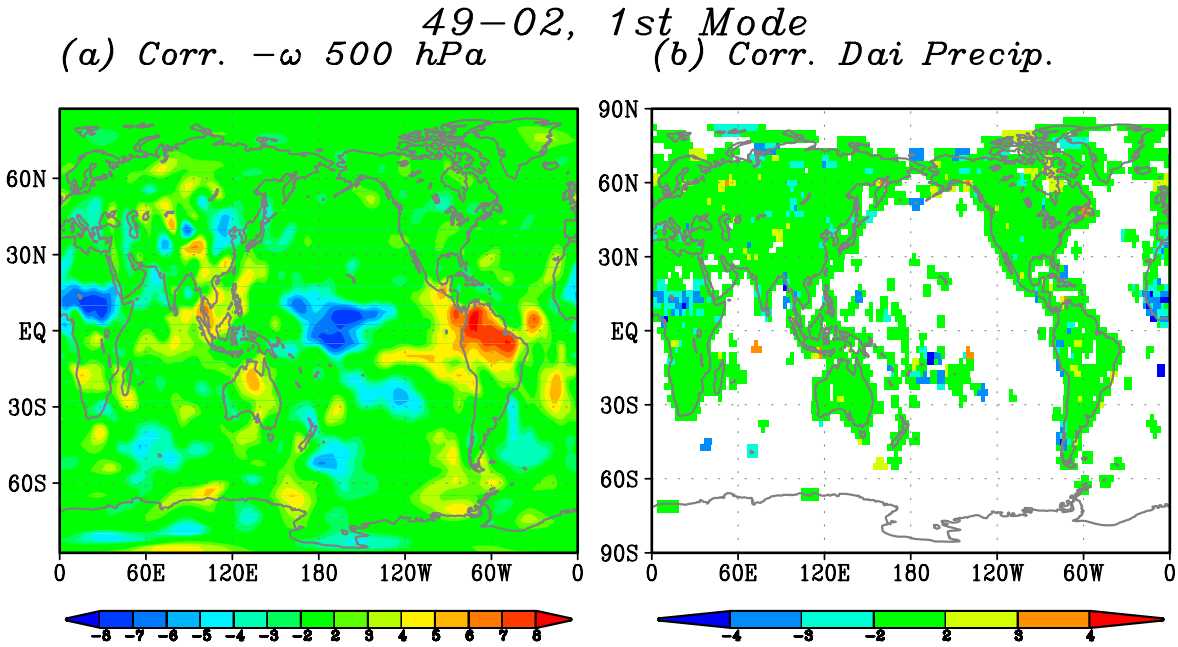

Figure. 11. (a) Correlations of the upward vertical velocity in the pressure coordinate at 500 hPa onto the PC-1 since 1949, which is shown in Fig. 8, and (b) correlations of the gauge precipitations onto the PC-1.